Cellular heterogeneity in pressure and growth emerges from tissue topology and geometry

Yuchen Long[1,*], Ibrahim Cheddadi[2,4], Vincent Mirabet[1], Gabriella Mosca[3], Mathilde Dumond[1,5], Jan Traas[1], Christophe Godin[1,2], Arezki Boudaoud[1,*].

1. Laboratoire Reproduction et Développement des Plantes, Université de Lyon, ENS de Lyon, UCB Lyon 1, CNRS, INRA, INRIA, F-69342, Lyon, France.

2. INRIA/CIRAD/INRA Project-team Virtual Plants, France.

3. Department of Plant and Microbial Biology, University of Zürich, Zollikerstrasse 107, CH-8008 Zürich, Switzerland.

4. Current address: Univ. Grenoble Alpes, CNRS, Grenoble INP, TIMC-IMAG, 38000 Grenoble, France.

5. Current address: Department of Biosystems Science and Engineering, ETH Zurich, Mattenstrasse 26, 4058, Basel, Switzerland.

*. Correspondence and requests for materials should be addressed to yuchen.long@ens-lyon.fr or arezki.boudaoud@ens-lyon.fr

The authors declare no competing financial interests.

Summary

Cell-to-cell fluctuations are observed in many biological phenomena like gene expression, signalling, cell size regulation and growth[1–8]. Notably, heterogeneity in cell size and growth rate often prevails and impacts tissue patterning and macroscopic growth robustness[1,2]. Cell volume change is driven by osmosis[9–11] and the resulting intracellular hydrostatic pressure, and is restrained by peripheral constraints (plasma membrane, cytoskeletal cortex, extracellular matrix, or cell wall) in plant[12], animal[13], tumorous[14] and microbial cells[15]. Despite numerous studies[15–17], the spatial variation of hydrostatic pressure in multicellular tissues, and its relation with cell-to-cell growth variability, remain elusive. Here, using micro-indentation by atomic force microscope, we demonstrate that hydrostatic pressure is

likely heterogeneous between adjacent cells in the epidermis of Arabidopsis shoot apical meristem. Combining experiments and physical modelling of cell wall mechanics and water movement, we propose that cell size and tissue topology contribute to the patterning of heterogeneities in pressure and growth, partially reminiscent of a liquid foam. Pressure correlates either positively or negatively with cellular growth rate depending on conditions, suggesting that the meristem is at a tipping point between limitation of growth by cell wall extensibility and by water conductivity. Together, our results shed light on spatial variations of pressure and growth rate, with potential roles in tissue homeostasis.

One sentence summary

Tissue geometry and topology induce heterogeneity in hydrostatic pressure and growth.

Key words

Cellular heterogeneity, hydrostatic pressure, tissue topology, growth mechanics, tissue hydraulics, atomic force microscopy, biophysical modelling.

Main text

Cell growth is driven by osmosis and constrained by cell envelope. Due to high difference between internal and external osmotic potential, cells with rigid cell walls – like in plants, bacteria and fungi – accumulate hydrostatic pressure, alias turgor pressure, often greater than atmospheric pressure (Extended Data Fig. 1)[12]. Animal cells also accumulate hydrostatic pressure, especially when compacted or contracting[13,14], though to a lesser extent than walled cells. In plants, turgor pressure is believed to positively correlate with growth rate, as depicted in the Lockhart-Ortega equation (Extended Data Fig. 1)[17]. However, observations suggest that growth rate and pressure level are not always associated[16], making it difficult to assess and understand the link between growth regulation and cellular pressure build-up. Here, we aimed at addressing this issue in a model plant tissue.

Recent advances in atomic force microscopy (AFM) enabled non-invasive turgor pressure retrieval utilizing indentation force-displacement and surface topography in living plant cells

(Fig. 1A)[18]. Accordingly, we used a pressurized thin-shell model to deduce the turgor pressure value from the AFM-measured force-displacement curve, which is influenced by turgor pressure, cell wall mechanical properties, and cell 3D geometry (Extended data Fig. 2; see Supplementary Discussion)[19]. We carefully evaluated the contributions of these parameters to the indentation results, and excluded many possible biases in deducing turgor from our AFM approaches (Extended data Fig. 2; see Supplementary Discussion). Additionally, influence of tissue context on indentation readout[22] was rigorously tested and ruled out by numerical simulations of indentations on realistic 3D meshes accounting for pressurized epidermal cells (Extended data Fig. 8; see Supplementary Discussion). Taken together, we concluded that our AFM measurements are sensitive to cell-to-cell turgor pressure variation, and semi-quantitative in regards to the absolute value of pressure. Accordingly, in the following, we use 'turgor pressure' to qualify the AFM-determined values.

We applied AFM-based pressure deduction to the epidermis of the *Arabidopsis thaliana* shoot apical meristem (SAM), a system featuring substantial growth heterogeneity[1]. We included untreated wild-type SAMs and a conceptually simpler model of chemically treated SAM that resembles a "foam of cells" (co-treated with naphthylphthalamic acid (NPA), a polar auxin transport inhibitor that induces pin-formed SAMs, and oryzalin, a microtubule-depolymerizing drug that blocks cell division but permits continuous, isotropic growth; hereafter referred to as "oryzalin-treated SAMs")[20]. Walls between cells are often curved in growing oryzalin-treated SAMs, like liquid films in a foam, suggesting that neighbouring cells have different turgor pressure[20] in a growing tissue (Extended Data Fig. 3). Cell-specific AFM measurements on nine SAMs revealed that turgor pressure is markedly heterogeneous in oryzalin-treated SAMs epidermis (Fig. 1E, Extended Data Fig. 2). Oryzalin-treated SAMs had average turgor pressures spanning the range 0.65 to 1.72 MPa (1.21 $\pm$ 0.34 MPa, mean $\pm$ standard error of mean; Extended Data Fig. 4). These values are comparable to the 2.0 MPa osmotic pressure estimated by incipient plasmolysis (Extended Data Fig. 5). The AFM-determined turgor also decreased with increasing osmolarity of external medium (Extended Data Fig. 5), further supporting this AFM-based approach.

Cell-specific measurements revealed that cellular pressure anticorrelates with the number of

epidermal cell-neighbours: cells with fewer neighbours have higher turgor pressure (Extended Data Fig. 6). We focused on cell-to-cell variations of turgor and we removed variations between SAMs by normalizing cellular pressure to the average pressure per SAM; normalized pressure decreases with neighbour number, being 1.3-fold greater in four- than in eight-neighboured cells (n = 202 cells, Pearson correlation coefficient R = -0.31, $p < 10^{-5}$) (Fig. 1F), consistent with previous prediction[20].

Untreated SAMs exhibit more constant turgor, as determined by AFM, at 2.62 ± 0.03 MPa (Extended Data Fig. 4), with the same magnitude as the estimated osmotic pressure at 1.2 MPa (Extended Data Fig. 5) and the preliminary values obtained previously[21] (see Supplementary Discussion). Consistently, we also detected similar, though slightly weaker, turgor–neighbour-number anticorrelation in untreated SAMs (7 SAMs, n = 503 cells, R = -0.16, $p = 10^{-4}$) (Fig. 1G-J, Extended Data Fig. 6, 7), confirming that non-random turgor pressure heterogeneity establish in tissues with static topology (no neighbour number change) or dynamic topology (neighbour numbers change due to division).

Earlier tissue models[20,23] treated intracellular pressure as an input or required differential osmotic pressure. Nevertheless, the anticorrelation that we find between pressure and neighbour number is reminiscent of liquid foams[24]. We therefore tested whether pressure heterogeneity could emerge from the classical plant water relations and wall mechanics[25] (Fig. 2A). We use a 2D vertex model, with topological distribution similar to SAM (Extended Data Fig. 9), that actually expands the Lockhart-Ortega equation of visco-elasto-plastic growth of single cell (Extended Data Fig. 1)[17] to cell walls in a multicellular tissue with more realistic 2D polygonal geometry. Each cell wall has a thickness w and behaves as an elastic material of modulus E when wall tension induced by turgor pressure P is low enough, more specifically when the elastic strain (ε, reversible deformation) is lower than a threshold ε^Y. When tension in the wall exceeds the corresponding threshold ($E\varepsilon^Y$), the cell wall undergoes irreversible expansion, akin to visco-plastic flow, with an extensibility (effective viscosity) Φ^w (Fig. 2A). Water flux from extracellular space is proportional to $L^a\Delta\Psi$, where $\Delta\Psi = \Delta\Pi - P$ is the cross-membrane water potential difference (external pressure is assumed to be zero; for the sake of simplicity we set $\Delta\Pi$ constant) and L^a is the conductivity. Intercellular water

redistribution via plant plasmodesmata[26], animal gap junctions, or cytoplasmic bridges[27,28] is driven by intercellular differences in turgor pressure P, with a conductivity L^s. We did not prescribe turgor pressure, instead letting it emerge from local mechanical and hydraulic interplays (see Methods for detailed model description).

Whereas cell wall extensibility can be more limiting for growth than water conductivity in fast elongating organs[29], we found that most aquaporin (channel protein allowing rapid water flux[30]) isoforms had significantly lower expression in inflorescence than in other fast growing tissues like stem and root[31] (with a reduction up to ~80%). Therefore we considered limitation of growth by cell wall extensibility and by water conductivity on equal footing. We first imposed slower water flux than cell wall extension, and found that, with homogenous effective parameters, we could recover the turgor–neighbour-number anticorrelation in our model, without or with cell divisions to mimic oryzalin-treated or untreated SAM (no division 5 simulations, n = 1219 cells, R = -0.87, $p < 10^{-100}$; dividing 8 simulations, n = 3240 cells, R = -0.58, $p < 10^{-100}$) (Fig. 2B-I). This implies that local hydrostatic pressure heterogeneity does not require differential cellular osmotic pressure[20] in a growing tissue, and predicts a topological origin of pressure variability, similar to liquid foams where pressure heterogeneity is due to fast liquid flow and limited gas diffusion rate between bubbles[24]. Indeed, water flow in a tissue parallels gas flow between cells in a foam and mechanics of cell walls replaces the rheology of the liquid films.

In order to test the robustness of this result, we explored the parameter space of the vertex model. Analytical exploration in a two-cell system[25] had showed that systems dynamics is controlled by two main dimensionless parameters, α^s, which compares intercellular water conductivity to total (intercellular and transmembrane) conductivity, and α^a, which compares the limitation of growth by transmembrane permeability to the combined limitation of growth by cell wall extensibility and transmembrane permeability (expression of these dimensionless parameters are given in the Methods). Accordingly, our first results, obtained with α^a = 0.1 and α^s = 0.1, denoted water flux-limited growth. We uplifted this limit, consistently with observations in many cell types[29], by increasing α^a from 0.1 to 0.5 and 0.9, where water conductivity equals or is relatively one magnitude higher than wall extensibility[32], and still

recovered the turgor–neighbour-number anticorrelation (Fig. 2J), demonstrating that strong flux limitation is not required for pressure heterogeneity. Next, we relaxed the intercellular flux limitation, by increasing α^s from 0.1 to 0.5 and 0.9, and showed that the anticorrelation is maintained even when intercellular flux is much stronger than osmotic water uptake (Fig. 2J). Shifting cell size checkpoint at division (by either -25% or +50%), which effectively changes average cell surface-to-volume ratio that antagonistically weighs the contribution of flux and wall limitations, also yields steady turgor–neighbour-number anticorrelation (Fig. 2J). Altogether, the parameter space exploration indicates that topology-related pressure heterogeneity is a robust outcome of the model.

In SAM surface, cell neighbour number and size are coupled (Extended Data Fig. 9). Consistently, cell-specific turgor pressure anticorrelates with normalized cell area (Extended Data Fig. 9). To uncouple cell size and topology, we modified the initial state of our simulation to have four-neighboured cells bigger than eight-neighboured cells, and found that higher turgor pressure accumulated in four-neighboured cells, not in the smaller cells (Extended Data Fig. 9), confirming that turgor pressure heterogeneity emerges from tissue topology rather than cell size differences. This can be explained by local topology, which determines cell wall angles and the subsequent tension distribution at each three-cell junction (Fig. 2K-N): in our model, wall stress and strain above the growth threshold are relaxed at a rate limited by wall extensibility and hydraulic conductivity. Therefore, stress and strain remain close to their values at growth threshold and are almost homogeneous in oryzalin-like simulations (Fig. 2C), and the sum of wall tension at each three-cell junction (vertex) mostly depends on the angles between walls. The vertex between three hexagonal cells with 120° internal angles has a sum of tension at zero (Fig. 2K, L). Fewer-neighboured cells have sharper internal angles, so the sum of tension at vertex is greater towards the cell interior, creating additional inward compression and prompting higher pressure build-up at equilibrium (Fig. 2M, N). In dividing simulations, as in the untreated case, new walls do not bear stress right after division because they form from cell interior. These new walls are gradually strained due to mesh growth but do not yield (expand) to release stress before reaching the threshold (Fig. 2G). Consequently, cell division keeps the wall stress from

homogenizing and dampens the turgor–neighbour-number anticorrelation (Fig. 2I). Notably, although tissue topology is sufficient to explain pressure heterogeneity, we do not exclude a role of other biological parameters and/or sources of noise in pressure variations, as suggested by weaker correlations in experiments (Fig. 1F, J) than in simulations. Nonetheless, since tissue topology is highly conserved in many biological systems[33], we propose that hydrostatic pressure heterogeneity may emerge in compact tissues with polygonal cells[34] and non-instantaneous water movement, due to the adjustment to reconcile local mechanical and hydraulic conditions.

Next, we monitored areal growth rate of SAM epidermal cells by time-lapse confocal microscopy. As observed previously, untreated SAMs exhibited slower growth in the central zone (CZ), where stem cells reside, than in the surrounding peripheral zone (PZ)[35] (Extended Data Fig. 7). In addition, cellular growth rate anticorrelates with neighbour number (11 SAMs, n = 1491 cells, R = -0.15, $p = 10^{-8}$; Fig. 3E) and cell size (Fig. 3F; R = -0.33, $p = 10^{-38}$), supporting previous reports that smaller cells in SAM grow faster[36,37], and suggests that higher turgor pressure in fewer-neighboured cells associates with faster growth. In oryzalin-treated SAMs, however, the fewer-neighboured and small cells grew slower (14 SAMs, n = 1160 cells; Fig. 3K, neighbour number R = 0.20, $p = 10^{-11}$; Fig. 3L, cell size R = 0.16, $p = 10^{-8}$). This suggests that higher turgor pressure associates with either faster or slower growth depending on conditions (Extended Data Fig. 9). Although seemingly a small shift, this negative-to-positive slope change of local growth heterogeneity captures a strong qualitative inversion of growth behaviour (Fig. 3D, J), where relative cell size increases exponentially in opposite fashions (Extended Data Fig. 10). Accordingly, smaller cells expand more than larger cells in untreated SAMs, which may contribute to cell size homeostasis, a phenomenon that would be absent in oryzalin-treated SAMs.

We further explored the growth trend in our vertex model. Based on the parameter exploration on dividing mesh aimed to reproduce untreated SAM behaviour, we found both positive and negative correlations between growth rate and cell neighbour number (Extended Data Fig. 11). This indicates that growth trend is sensitive to parameters that alter the balance between water flux and wall expansion. Conservatively, we chose equal contribution by flux and wall in our

model (α^a = 0.5), which required scaling up theoretical cell size (by +50%) to maintain growth trend as in untreated SAM: Figures 4A-C show that the fewer-neighboured and smaller cells grow faster (10 simulations, n = 5971; G vs N, R = -0.25, $p = 10^{-84}$; G vs A, R = -0.96, $p < 10^{-100}$).

We then attempted to reproduce oryzalin-treated behaviour, guided by the experimental observations that, besides stopping cell division, oryzalin treatment also yields higher osmotic pressure (1.6-fold) and drastically thicker cell walls (4-fold) (Extended Data Fig. 5, 12). We found that both stalling division and increasing osmotic pressure failed to invert the growth trend in the model, while doubling and quadrupling wall thickness inverted the correlation of growth rate to neighbour number and cell size (Fig. 4D-F, G; Extended Data Fig. 13), like in oryzalin-treated SAM. Combining higher osmotic pressure and thicker wall revealed that quadrupling wall thickness can robustly trigger growth trend inversion (Fig. 4, Extended Data Fig. 13).

Effectively, changing osmotic pressure and wall thickness also alters the wall–flux limitation balance of the system (Fig. 4G). Higher osmotic pressure induces faster water influx (reduced limitation by flux). The extra volume strains the walls to accumulate stress farther beyond the threshold, which is relaxed by wall yielding (growth) with extensibility as the rate limit. Meanwhile, wall thickening reduces wall stress and strain towards the threshold for expansion, effectively reducing the mechanical drive of growth and increasing the weight of water permeability in limiting growth, similar to liquid foam. We do not exclude other possible parameter changes triggered by oryzalin treatment, like water conductivity and wall synthesis rate, that also contribute to the wall–flux limitation balance. Nevertheless, implementing the observed cell wall thickening in the model is sufficient to explain the observed growth rate inversion from untreated to oryzalin-treated scenario.

Together, we propose that tissue mechanics and hydraulics act in parallel with the established genetic regulations in SAM cell growth. We demonstrate that cellular hydrostatic pressure is innately heterogeneous in Arabidopsis SAM epidermis; however, it is not a proxy of local growth rate variability, contrary to expectations. Instead, our analysis suggests that turgor

pressure and growth rate are combinatorial outputs of local mechanics and hydraulics. Each of these parameters can be controlled by genetic and biochemical inputs, and small uniform changes in these biological inputs can enable drastic shifts of cell size distribution (Extended Data Fig. 14), unlike liquid foams in which cell size distribution always enlarge over time. Our simulation and experiment data suggest that Arabidopsis SAM is likely close to the tipping point between the limits of wall synthesis and water influx. Such inversion in growth trend is not irrelevant to normal development: for example, a growth variability switch is observed during sepal development, where clones of smaller and often fewer-neighboured cells grow faster in young sepals then slower in older sepals, effectively switching from homogenizing to amplifying cell size variability[38]. The emergent heterogeneity of local growth and hydrostatic pressure likely underlies morphogenesis in other compact tissues with polygonal cells.

Acknowledgements

We thank P. Bolland and A. Lacroix for plant care, G. Cloarec for help with TEM, L. Beauzamy for AFM training, C. Mollier for help in estimating confocal technical errors, A. Kiss for help with anisotropic filtering parameterization, G. Cerrutti for help in implementing the division algorithm and in segmentation and mesh generation for the indentation simulations, and R. Smith for help in segmentation and mesh generation for the indentation simulations. We acknowledge the contribution of the PLATIM facility of SFR Biosciences (UMS3444/CNRS, US8/Inserm, ENS de Lyon, UCBL) for AFM and confocal microscopy, and of Centre Technologique des Microstructures (UCBL, Lyon) for electron microscopy. This work was supported by a fellowship from Institut Universitaire de France and an ERC Starting Grant “PhyMorph” to A.B. (ERC-2012-StG-307387), an EMBO Long-term Fellowship to Y.L. (EMBO ALTF 168-2015), and an Agropolis Foundation grant (MecaFruit3D) to I.C. and C.G.

Author contributions

This study was initiated by A.B. Y.L. and A.B. designed the experiments. Y.L. executed AFM and confocal microscopy, acquired experimental data except EM, and analysed experimental

and simulation data. J.T. performed electron microscopy. V.M and M.D. wrote scripts to facilitate experimental data analysis. I.C. and C.G. designed physical model of tissue growth. I.C. implemented the model, ran simulations, optimized model parameters and analysed simulation data. G.M. designed, ran, and analysed indentation simulations. Y.L. and A.B. contributed to the design of simulations. Y.L., I.C., V.M., G.M., C.G. and A.B. contributed to data interpretation. Y.L. and A.B. wrote the manuscript with inputs from the other authors.

Figures

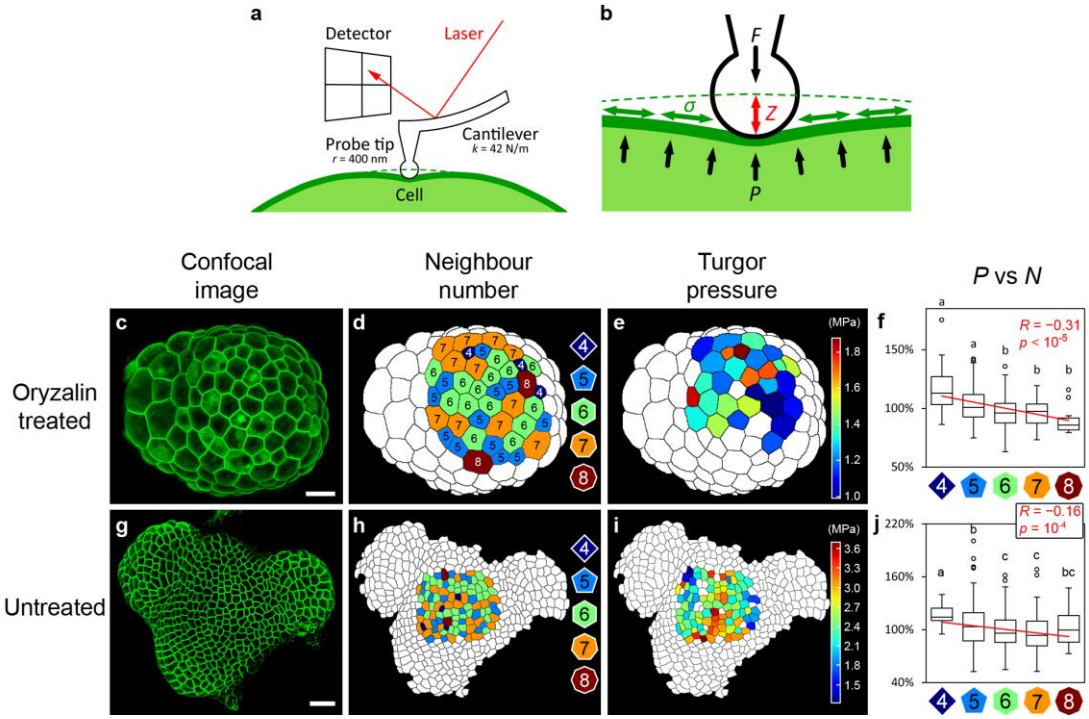

Figure 1. Turgor pressure heterogeneity in SAM is associated with variation of cell topology.

(**a** and **b**) Schematic representation of AFM nanoindentation for turgor pressure measurement. *r*, probe tip radius; *k*, cantilever stiffness; *F*, indentation force; *Z*, indentation depth; *P*, turgor pressure; *σ*, cell wall tension. (**c** to **j**) Cell-specific turgor pressure in oryzalin-treated (c to f) and untreated SAM (g to j). (c and g) Top-view surface projections of SAM, oryzalin-treated (c) or untreated (g), with plasma membrane GFP signal; scale bars represent 20 µm. (d and h) Cell topology determined on segmented cell contour images, around SAM centre; numbers indicate neighbour number in epidermis. (e and i) AFM-determined cell-specific turgor pressure heat maps. (f and j) Box plots of cellular turgor pressure *P* normalized per SAM against cell topology *N* (f, oryzalin-treated 9 SAMs, *n* = 202 cells; j, untreated 7 SAMs, *n* = 503 cells). Circles are Tukey's outliers; lowercase letters indicate statistically different populations (Student's *t*-test, $p < 0.05$); red lines indicate linear regressions, with Pearson correlation coefficient *R* and corresponding *p*-value.

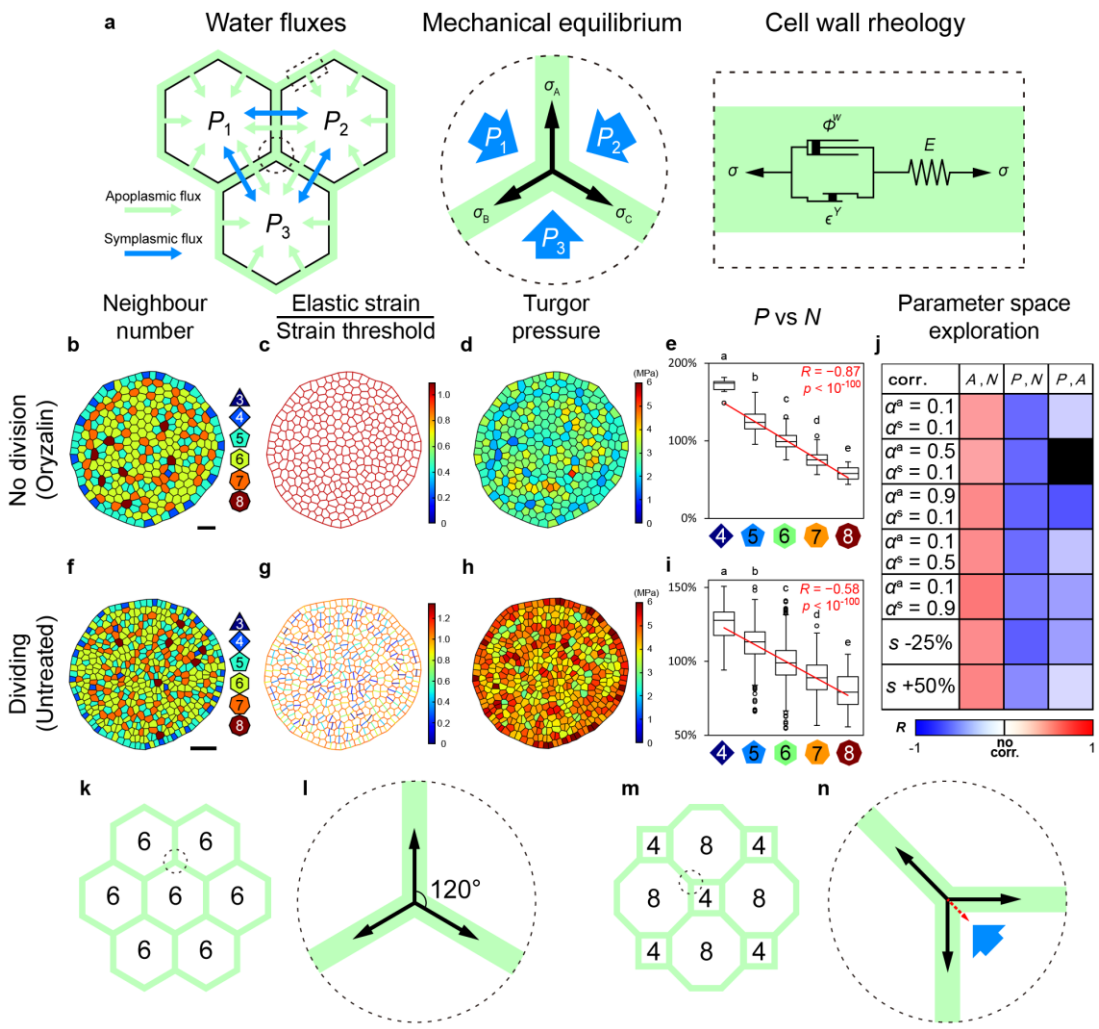

Figure 2. Turgor pressure heterogeneity emerges from cell topology.
(**a**) Schematic representations of model components, including apoplasmic and intercellular water fluxes (left), mechanical equilibrium at three-cell junctions (middle) and the visco-elasto-plastic cell wall rheology. *P*, cell-specific turgor pressure; σ, cell wall tension; Φ^w, wall extensibility; ϵ^Y, wall strain threshold; *E*, wall Young's modulus. (**b** to **i**) Turgor pressure in non-dividing (oryzalin-treated, b to e) and dividing (untreated) simulations (f to i), scale bars are 5 unit length. (b and f) Cell topology; (c and g) cell wall strain relative to strain threshold; (d and h) cellular turgor pressure heat maps; (e and i) Box plots of normalized cellular turgor pressure *P* against cell topology *N* (d, non-dividing 5 simulations, n = 1219 cells; g, dividing 8 simulations, n = 3240 cells). Cells on the mesh edge were not analysed due to border effect. Circles are Tukey's outliers; lowercase letters indicate statistically different populations (Student's *t*-test, $p < 0.05$); red lines indicate linear regressions, with Pearson correlation coefficient *R* and corresponding *p*-value. (**j**) Model parameter exploration. Colours indicate Person correlation *R*, with perfect anticorrelation as blue (R = -1), perfect correlation in red (R = 1), and insignificant correlation ($p > 0.05$) in black. *A*, normalized cell area; *N*, cell neighbour number; *P*, normalized turgor pressure; α^a, dimensionless parameter for flux-wall limit balance; α^s, dimensionless parameter for apoplasmic-symplasmic limit balance; *s*, cell size at division (**k** to **n**) Schematic explanation

of topology-derived turgor pressure heterogeneity. (k and l) Three-cell junctions in a tissue of hexagonal cells are at mechanical equilibrium with equal tensions and equal wall-wall angles. (m and n) Fewer-neighboured cells have sharper wall-wall angles, a tension that is roughly constant per wall effectively results in mechanical compression due to unequal projected tension distribution (red dash-line arrow) that is balanced by higher turgor pressure build-up (big blue arrow).

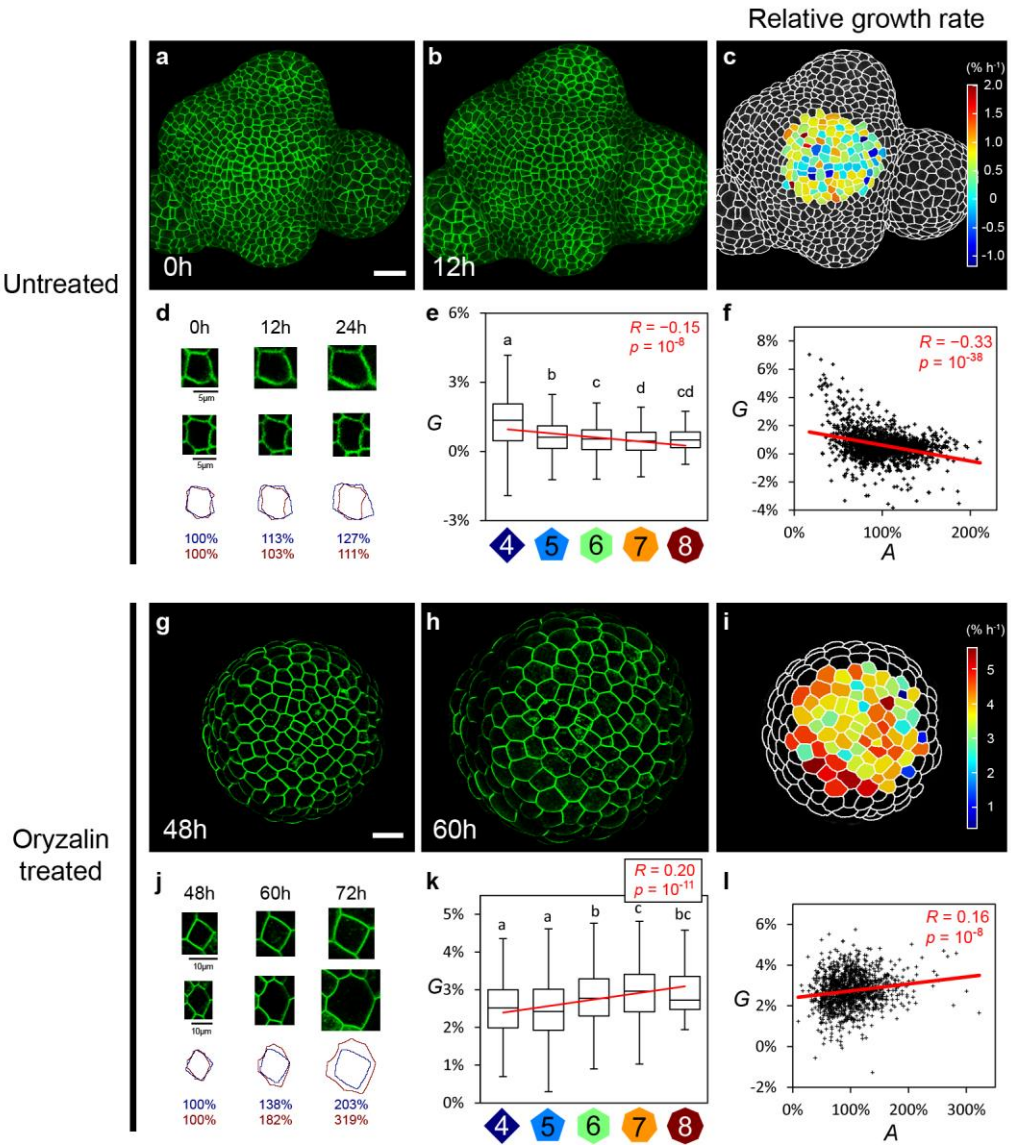

Figure 3. Cellular growth rate bifurcates between conditions.

(**a** to **f**) Relative growth rate per hour *G* of untreated SAM cells between 12-hour interval. (**g** to **l**) Cellular growth rate per hour of oryzalin-treated SAM between 12-hour interval (48 and 60 hours post treatment). (a, b, g and h) Surface projections of untreated or oryzalin-treated SAM at initial time point (a and g) and 12 hours later (b and h); scale bars are 20 µm unless otherwise noted. (c and i) Heat maps of areal relative growth rate per hour. (d and j) Example 4 and 8-neighbored cells during 24-hour growth, with areal normalization at initial time point. Cell contour and relative size (blue for 4-neighbored, red for 8-neighbored) depict the diverging growth trends. Scale bars are as indicated. (e, f, k and l) Box plots of relative

growth rate per hour G against cell topology N (e and k) and dot plots of relative growth rate per hour G against normalized cell area A (f and l) (e and f, untreated 11 SAMs, n = 1491 cells; k and l, oryzalin-treated 14 SAMs, n = 1160 cells). Note that Tukey's outliers are not plotted, but are included for statistical analyses. Lowercase letters indicate statistically different populations (Student's t-test, $p < 0.05$); red lines indicate linear regressions, with Pearson correlation coefficient R and corresponding p-value.

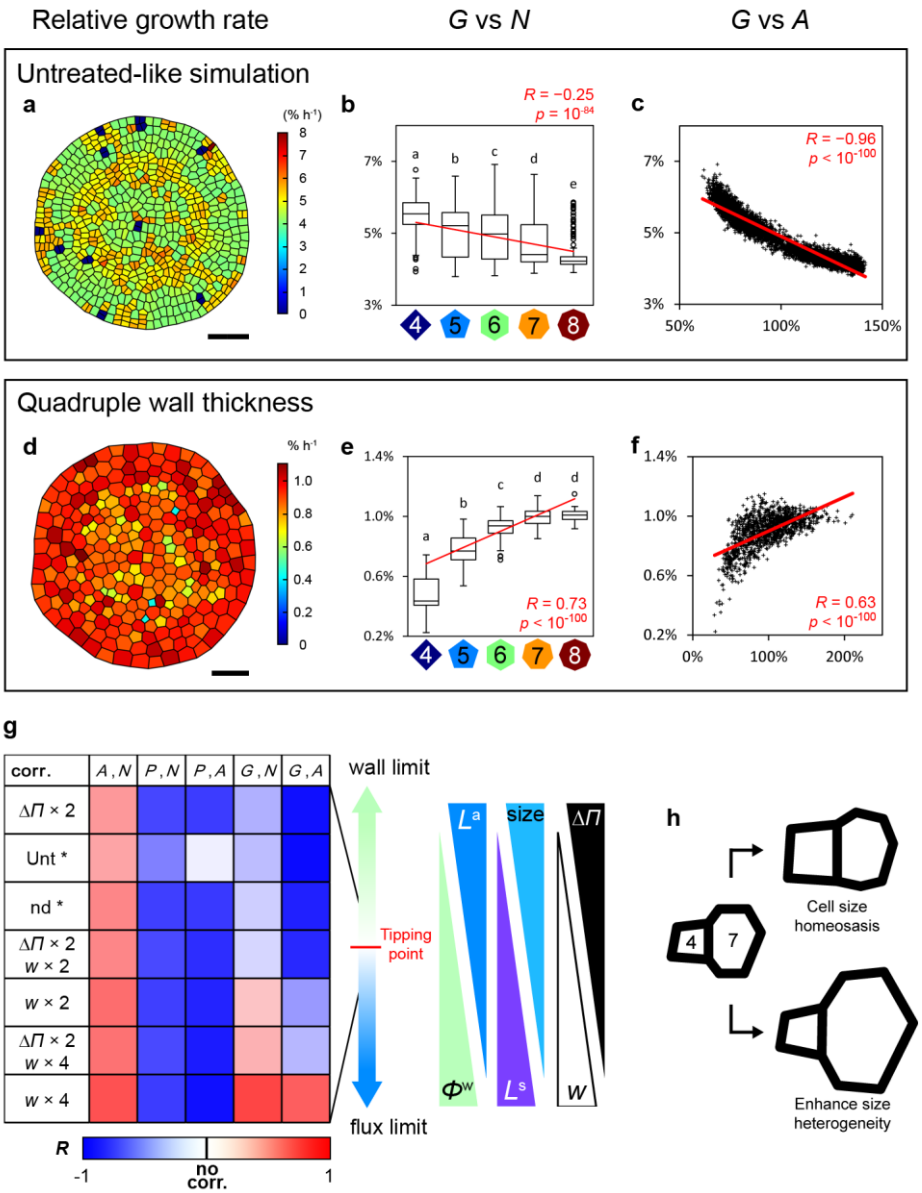

Figure 4. Model effective parameters that enable recapitulating the untreated and oryzalin-treated growth trends.

(**a** to **c**) Relative growth rate per hour G in simulations with cell division, which corresponds to α^a = 0.5 and division size s +50%, and mimics untreated SAM. Cells that just divided (dark blue with 0 growth) are not included in analysis. (**d** to **f**) Growth simulations with no cell division, α^a = 0.5, and quadruple wall thickness to mimic oryzalin treatment. (a, d) Heat maps of areal relative growth rate per hour. Scale bars are 10 unit lengths. (b, e) Box plots of relative growth rate per hour G against cell topology N. Lowercase letters indicate statistically

different populations (Student's *t*-test, $p < 0.05$); red lines indicate linear regressions, with Pearson correlation coefficient R and corresponding p-value. (c, f) Dot plots of relative growth rate per hour G against normalized cell area A. Numbers of repeats see Methods. (**g**) Model exploration to fit oryzalin-treated case. Colours indicate Person correlation R, with perfect anticorrelation as blue (R = -1), perfect correlation in red (R = 1), and insignificant correlation ($p > 0.05$) in black. Triangles indicate parameter's influence to the flux-wall limit balance. * indicates the same parameter choices ($\alpha^{a} = 0.5$ and division size s +50%), with Unt indicating dividing, untreated-like simulations and nd for non-dividing; $\Delta\Pi$, osmotic drive; w, wall thickness; A, normalized cell area; N, cell neighbour number; P, normalized turgor pressure; G, relative growth rate; Φ^{w}, wall extensibility; L^{a}, cross-membrane water conductivity; L^{s}, cell-to-cell symplasmic conductivity; size, cell size at division. (**h**) Summary of growth trend inversion according to the flux-wall limits shown in (g).

References

1. Hong, L. *et al.* Heterogeneity and Robustness in Plant Morphogenesis: From Cells to Organs. *Annu. Rev. Plant Biol.* **69**, 469–495 (2018).
2. Kamimoto, K. *et al.* Heterogeneity and stochastic growth regulation of biliary epithelial cells dictate dynamic epithelial tissue remodeling. *eLife* **5**, (2016).
3. Ietswaart, R., Rosa, S., Wu, Z., Dean, C. & Howard, M. Cell-Size-Dependent Transcription of FLC and Its Antisense Long Non-coding RNA COOLAIR Explain Cell-to-Cell Expression Variation. *Cell Syst.* **4**, 622-635.e9 (2017).
4. Long, Y. *et al.* In vivo FRET-FLIM reveals cell-type-specific protein interactions in Arabidopsis roots. *Nature* **548**, 97–102 (2017).
5. Chubb, J. R. Symmetry breaking in development and stochastic gene expression. *Wiley Interdiscip. Rev. Dev. Biol.* **6**, e284 (2017).
6. Donati, G. & Watt, F. M. Stem Cell Heterogeneity and Plasticity in Epithelia. *Cell Stem Cell* **16**, 465–476 (2015).
7. Gerdes, M. J. *et al.* Emerging Understanding of Multiscale Tumor Heterogeneity. *Front. Oncol.* **4**, (2014).
8. Eldar, A. & Elowitz, M. B. Functional roles for noise in genetic circuits. *Nature* **467**, 167–173 (2010).
9. Watanabe, K., Umeda, T., Niwa, K., Naguro, I. & Ichijo, H. A PP6-ASK3 Module Coordinates the Bidirectional Cell Volume Regulation under Osmotic Stress. *Cell Rep.* **22**, 2809–2817 (2018).
10. Xie, K., Yang, Y. & Jiang, H. Controlling Cellular Volume via Mechanical and Physical Properties

284 of Substrate. *Biophys. J.* **114**, 675–687 (2018).

285 11. Guo, M. *et al.* Cell volume change through water efflux impacts cell stiffness and stem cell
286 fate. *Proc. Natl. Acad. Sci.* **114**, E8618–E8627 (2017).

287 12. Dumais, J. & Forterre, Y. "Vegetable Dynamicks": The Role of Water in Plant Movements.
288 *Annu. Rev. Fluid Mech.* **44**, 453–478 (2012).

289 13. Stewart, M. P. *et al.* Hydrostatic pressure and the actomyosin cortex drive mitotic cell
290 rounding. *Nature* **469**, 226–230 (2011).

291 14. Montel, F. *et al.* Stress clamp experiments on multicellular tumor spheroids. *Phys. Rev. Lett.*
292 **107**, 188102 (2011).

293 15. Rojas, E. R. & Huang, K. C. Regulation of microbial growth by turgor pressure. *Curr. Opin.*
294 *Microbiol.* **42**, 62–70 (2017).

295 16. Kroeger, J. H., Zerzour, R. & Geitmann, A. Regulator or driving force? The role of turgor
296 pressure in oscillatory plant cell growth. *PloS One* **6**, e18549 (2011).

297 17. Ortega, J. K. Augmented growth equation for cell wall expansion. *Plant Physiol.* **79**, 318–320
298 (1985).

299 18. Beauzamy, L., Derr, J. & Boudaoud, A. Quantifying Hydrostatic Pressure in Plant Cells by Using
300 Indentation with an Atomic Force Microscope. *Biophys. J.* **108**, 2448–2456 (2015).

301 19. Vella, D., Ajdari, A., Vaziri, A. & Boudaoud, A. The indentation of pressurized elastic shells:
302 from polymeric capsules to yeast cells. *J. R. Soc. Interface* **9**, 448–455 (2012).

303 20. Corson, F. *et al.* Turning a plant tissue into a living cell froth through isotropic growth. *Proc.*
304 *Natl. Acad. Sci. U. S. A.* **106**, 8453–8458 (2009).

305 21. Beauzamy, L., Louveaux, M., Hamant, O. & Boudaoud, A. Mechanically, the Shoot Apical

306 Meristem of Arabidopsis Behaves like a Shell Inflated by a Pressure of About 1 MPa. *Front.*
307 *Plant Sci.* **6**, (2015).
308 22. Mosca, G., Sapala, A., Strauss, S., Routier-Kierzkowska, A.-L. & Smith, R. S. On the
309 micro-indentation of plant cells in a tissue context. *Phys. Biol.* **14**, 015003 (2017).
310 23. Ishihara, S. *et al.* Comparative study of non-invasive force and stress inference methods in
311 tissue. *Eur. Phys. J. E Soft Matter* **36**, 9859 (2013).
312 24. Weaire, D. L. & Hutzler, S. *The Physics of Foams*. (Clarendon Press, 2001).
313 25. Cheddadi, I., Genard, M., Bertin, N. & Godin, C. Coupling water fluxes with cell wall
314 mechanics in a multicellular model of plant development. *bioRxiv* 511717 (2019).
315 doi:10.1101/511717
316 26. Lucas, W. J., Ham, B.-K. & Kim, J.-Y. Plasmodesmata - bridging the gap between neighboring
317 plant cells. *Trends Cell Biol.* **19**, 495–503 (2009).
318 27. Kumar, N. M. & Gilula, N. B. The Gap Junction Communication Channel. *Cell* **84**, 381–388
319 (1996).
320 28. McLean, P. F. & Cooley, L. Protein Equilibration through Somatic Ring Canals in Drosophila.
321 *Science* **340**, (2013).
322 29. Cosgrove, D. J. Wall extensibility: its nature, measurement and relationship to plant cell
323 growth. *New Phytol.* **124**, 1–23 (1993).
324 30. Maurel, C. *et al.* Aquaporins in Plants. *Physiol. Rev.* **95**, 1321–1358 (2015).
325 31. Klepikova, A. V., Kasianov, A. S., Gerasimov, E. S., Logacheva, M. D. & Penin, A. A. A high
326 resolution map of the Arabidopsis thaliana developmental transcriptome based on RNA-seq
327 profiling. *Plant J. Cell Mol. Biol.* **88**, 1058–1070 (2016).

32. Ortega, J. K. E. Dimensionless Numbers to Analyze Expansive Growth Processes. *Plants* **8**, 17 (2019).

33. Gibson, W. T. & Gibson, M. C. Chapter 4 Cell Topology, Geometry, and Morphogenesis in Proliferating Epithelia. in *Current Topics in Developmental Biology* **89**, 87–114 (Academic Press, 2009).

34. Péret, B. *et al.* Auxin regulates aquaporin function to facilitate lateral root emergence. *Nat. Cell Biol.* **14**, 991–998 (2012).

35. Kwiatkowska, D. Surface growth at the reproductive shoot apex of Arabidopsis thaliana pin-formed 1 and wild type. *J. Exp. Bot.* **55**, 1021–1032 (2004).

36. Serrano-Mislata, A., Schiessl, K. & Sablowski, R. Active Control of Cell Size Generates Spatial Detail during Plant Organogenesis. *Curr. Biol.* **25**, 2991–2996 (2015).

37. Willis, L. *et al.* Cell size and growth regulation in the Arabidopsis thaliana apical stem cell niche. *Proc. Natl. Acad. Sci. U. S. A.* **113**, E8238–E8246 (2016).

38. Tsugawa, S. *et al.* Clones of cells switch from reduction to enhancement of size variability in Arabidopsis sepals. *Development* **144**, 4398–4405 (2017).

Methods references

39. Cutler, S. R., Ehrhardt, D. W., Griffitts, J. S. & Somerville, C. R. Random GFP∶∶cDNA fusions enable visualization of subcellular structures in cells of Arabidopsis at a high frequency. *Proc. Natl. Acad. Sci.* **97**, 3718–3723 (2000).

40. Stanislas, T., Hamant, O. & Traas, J. Chapter 11 - In-vivo analysis of morphogenesis in plants. in *Methods in Cell Biology* (ed. Lecuit, T.) **139**, 203–223 (Academic Press, 2017).

41. Reuille, P. B. de, Bohn-Courseau, I., Godin, C. & Traas, J. A protocol to analyse cellular dynamics during plant development. *Plant J.* **44**, 1045–1053 (2005).

42. Legland, D., Arganda-Carreras, I. & Andrey, P. MorphoLibJ: integrated library and plugins for mathematical morphology with ImageJ. *Bioinformatics* **32**, 3532–3534 (2016).

43. Mirabet, V. *et al.* NanoIndentation, an ImageJ Plugin for the Quantification of Cell Mechanics. *Methods Mol. Biol.* (in press).

44. Sassi, M. *et al.* An auxin-mediated shift toward growth isotropy promotes organ formation at the shoot meristem in Arabidopsis. *Curr. Biol. CB* **24**, 2335–2342 (2014).

45. Kremer, A. *et al.* Developing 3D SEM in a broad biological context. *J. Microsc.* **259**, 80–96 (2015).

46. Reuille, P. B. de *et al.* MorphoGraphX: A platform for quantifying morphogenesis in 4D. *eLife* **4**, e05864 (2015).

47. Kiss, A. *et al.* Segmentation of 3D images of plant tissues at multiple scales using the level set method. *Plant Methods* **13**, 114 (2017).

48. Schmidt, T. *et al.* The iRoCS Toolbox – 3D analysis of the plant root apical meristem at cellular resolution. *Plant J.* **77**, 806–814 (2014).